Arabian Journal of Chemistry 16 (2023) 105243

Contents lists available at ScienceDirect

Arabian Journal of Chemistry

journal homepage: www.sciencedirect.com

Original article

Research on pitting corrosion characteristics of X90 steel based on acoustic emission and electrochemistry methods

Haisheng Bi [a,*], Jiaxu Miao [a], Zhifeng Sun [b], Yuhong Zhang [a], Yangyang Zhou [a], Chen Zhang [a], Chunxun Ma [a], Huiyao Li [a]

[a] College of Electromechanical Engineering, Qingdao University of Science & Technology, Qingdao 266061, China
[b] Sinopec Petroleum Engineering Corporation, Dongying 257000, China

ARTICLE INFO

Article history:
Received 27 February 2023
Accepted 3 September 2023
Available online 6 September 2023

Keywords:
X90 pipeline steel
Pitting Corrosion
Acoustic emission
Electromechanical
Wavelet analysis

ABSTRACT

The X90 pipeline steel pipe is expected to become the standard steel in future pipeline construction due to its high transmission efficiency and lower cost. However, little study has been conducted on corrosion on-line monitoring of X90 steel. To investigate the pitting development of X90 steel, a combined electrochemical device and acoustic emission (AE) system was set up in this work. The results reveal that the pitting process can be divided into three stages: activation response and passive film rupture, and corrosion pit propagation, and pitting reaction. In addition, the corrosion rate of metal is quite high during the activation reaction and passivation film rupture stage, and the characteristic parameters of the AE signal are very large. In the frequency domain, the frequency range is mostly centered between 100 and 200 kHz, with a peak frequency of about 150 kHz. The corrosion pit propagation stage is the transition stage from metal oxidation to metal pitting reaction. The activity of the signal is low, and the characteristic signal is diminished, and the frequency domain characteristics are comparable to the preceding stage. The signal activity rises, the total signal intensity increases, and several signals exceeding 55 dB arise during the pitting response stage.

1. Introduction

The trend of global oil and gas pipeline construction and development is to create long-distance, high-pressure, large-capacity transportation pipelines, which require high-grade, large-diameter, and thick-walled steel (Wang et al., 2022; Bhardwaj et al., 2021; Feng et al., 2021). By 2020, X80 pipeline steel has become the most widely utilized type of pipeline steel in China. The overall distance of built pipelines is around 17,000 km, placing the country top in the world (Wang et al., 2022; Luguang, 2022; Chen et al., 2021). In the future, X90 pipeline steel and higher grade X120 pipeline steel are predicted to become the standard pipeline steel (Luo et al., 2019; Luo et al., 2016; Eliyan et al., 2012). However, oil and gas pipeline corrosion has had a significant effect on energy transportation safety. Pitting corrosion is one of the most common types of corrosion incidents in pipelines, and should be given more consideration in pipeline safety studies (Feng et al., 2021; Seghier et al., 2020; Li et al., 2023). For example, pipeline pitting corrosion perforation was the major cause of the '11·22′ leakage and explosion accident of Sinopec Donghuang crude oil pipeline in Qingdao, China.

Modern physical and chemical immersion, electrochemical tests, AE monitoring, and other nondestructive testing procedures are used to analyze pitting corrosion. Mingjie Dai et al. (Dai et al., 2018) used SWP (square wave polarization) technology in conjunction with potentiodynamic polarization, field scanning electron microscopy (FE-SEM), and theoretical calculations to investigate the pitting corrosion of X100 pipeline steel in acid soil solution, the results demonstrate that pitting corrosion can occur on the cathodically polarized steel and primarily produce on the steel matrix rather than non-metallic inclusions. Zhuowei Tan et al. (Tan et al., 2020) used electrochemical impedance spec-

* Corresponding author : Doctor of Oil and Gas Storage and Transportation Engineering, Associate Professor, Researcher at College of Electromechanical Engineering, Qingdao University of Science & Technology, Qingdao 266061, China.
E-mail addresses: bhs888796@163.com, bhs888796@qust.edu.cn (H. Bi), mjx040017@163.com (J. Miao), sunzf.osec@sinopec.com (Z. Sun), 3451086638@qq.com (Y. Zhang), zyy080997@163.com (Y. Zhou), zhangchenczc@163.com (C. Zhang), 884870426@qq.com (C. Ma), Missmissli@126.com (H. Li).
Peer review under responsibility of King Saud University.

Production and hosting by Elsevier

https://doi.org/10.1016/j.arabjc.2023.105243

troscopy (EIS), scanning electron microscopy (SEM), x-ray diffraction (XRD), and energy dispersive spectroscopy (EDS) to investigate the features of corrosion products on the specimen surface in CO_2-saturated NACE solution (EDS). They found that the local defect-induced flow field has a considerable effect on the composition and micromorphology of corrosion scales in various regions. Fregonese M. et al. (Fregonese et al., 2001) investigated the corrosion process of 316L stainless steel in NaCl solution with pH = 2, as well as the related AE signal characteristics, and found that the corrosion mode of 316L stainless steel in this environment shifted from pitting to uniform corrosion. Hong Ju et al. (Ju et al., 2021) used simultaneous electrochemical measurement and imaging technologies to investigate the pitting corrosion and hydrogen evolution processes of aluminum and AA2024 alloy. In addition, Kaige Wu (Wu and Kim, 2021) investigated the AE sources related to the open morphology of pitting; Zhan Zhang et al. (Zhang et al., 2021) used electrochemical noise and AE technology to monitor the pitting corrosion of AZ31 magnesium alloy, providing a feasible method for effectively monitoring the self-corrosion process of magnesium alloy. Jian Xu et al. (Xu et al., 2011) investigated the AE performance of the 304 steel pitting process at various acid-base and ion concentrations, and found that the activity of the AE signal was discovered to correlate with pH value but has minimal association with Cl^- concentration.

The research object in this work is high-strength X90 pipeline steel, and the X90 pipeline steel pitting corrosion properties are investigated. To effectively identify the type and degree of corrosion, the characteristics of AE signals under different corrosion degrees were extracted, combined with electrochemical detection and morphological observation. The results can provide theoretical support for online AE detection of pipeline corrosion and defect identification, and further ensure safe pipeline operation.

2. Experimental process

2.1. Materials

The experimental material was X90 high-strength pipeline steel obtained from the field pipelines, and the X90 steel composition is shown in Table 1.

The specimen size was measured as 32 mm × 35 mm × 3 mm (±0.1 mm), and the specimen sliced with steel wire and covered with epoxy resin adhesive and ground to a dazzling mirror surface.

2.2. The experimental medium

The pH of 1500 mL NaCl solution with 3% mass fraction and 0.1 mol/L standard HCl was adjusted to 3.0 as the corrosion medium in this experiment.

2.3. AE-electrochemical joint experimental system

As illustrated in Fig. 1, the experimental system was a square glass fiber-reinforced plastic container with dimensions of 220 mm × 220 mm × 75 mm and a thickness of 10 mm. The container had a 38 mm × 38 mm × 5 mm inner hole and a 55 mm × 55 mm × 5 mm outer hole in the center of the bottom. The encapsulated specimen can be embedded in the step hole. When the working surface came into contact with the corrosive solution through the inner hole, the AE sensor was placed at the bottom of the specimen, and the reference electrode and a platinum electrode were placed on the three-electrode cell (Bi, n.d.). The platinum electrode and the reference electrode were arranged along two sides of the perforated plate to maintain corrosive solution balance and to successfully avoid the interference of the hydrogen bubble. Fig. 1 depicts the experimental system.

Physical Acoustics Corporation (PAC) manufactures the AE acquisition system, which enables real-time capture and processing, as demonstrated in Fig. 2. As illustrated in Fig. 3, the electrochemical system is set up by AMETEK and can be adapted to the open software Power Suite to fulfill the experimental needs of a wide variety of specimens.

3. Results and discussion

3.1. Pitting potential and analysis

The potentiodynamic polarization experiment was set to range from −0.25 V (vs. OCP) to 1.60 V at a scan rate of 0.5 mV/s. The potentiodynamic polarization curve for the X90 steel pitting exper-

Table 1
X90 steel chemical composition (weight percent %).

Specimen	Chemical composition								
	Mn	Ni	Mo	Si	Cu	Cr	Nb	C	Ti + P + V + S	Fe
X90	1.72	0.33	0.29	0.26	0.24	0.24	0.08	0.05	<0.03	balance

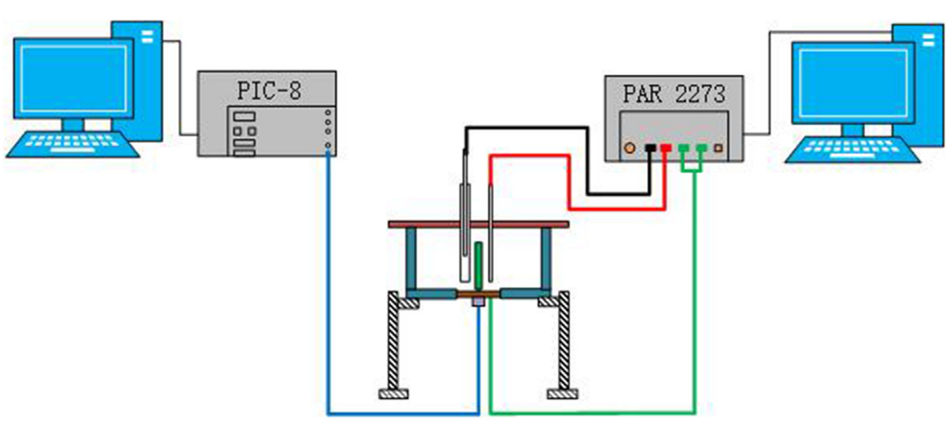

Fig. 1. Pitting corrosion experimental device.

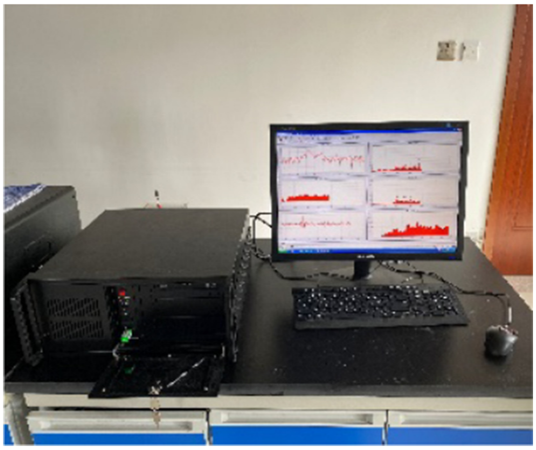

Fig. 2. PCI-8 acoustic emission system.

Fig. 3. Electrochemical system.

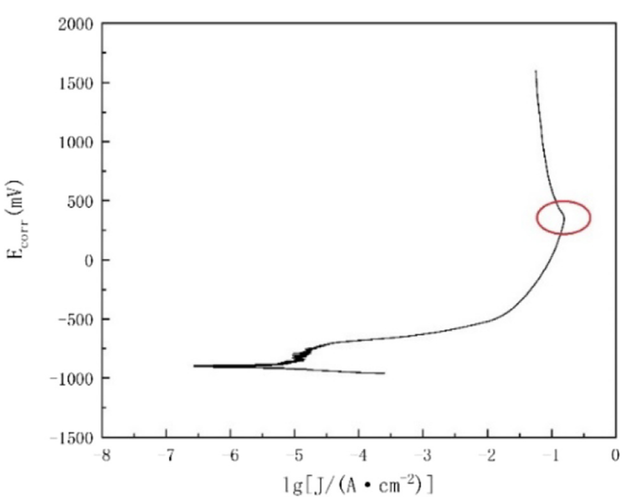

Fig. 4. Potentiodynamic Polarization Curve of X90 Steel in NaCl Solution with pH = 3.0.

iment is shown in Fig. 4. The circle (see Fig. 4) means that as the potential scans to about 400 mV, the current density suddenly decreases.

Weak bubbles start to form close to the platinum electrode when the scanning potential hits about −584 mV, as shown in Fig. 5(a). As shown in Fig. 5(b), after approximately 600 s, bubbles are violently generated and diffuse upwards from the platinum sheet. A thin and dense oxide film develops on the specimen's surface as the scanning potential rises. The current density rapidly decreases at a potential sweep of around 400 mV, indicating the formation of the passive film, which has a protect effect that lowers the current density and reduced corrosion current density. The potentiodynamic polarization curve becomes straight as the voltage rises, suggesting that the current density is constant and the passivation film's obstruction is still present and the passive film also continues to thicken as the voltage rises. The phenomena of passive film exfoliation close to the specimen is seen around 1000 to 1300 mV. The passive film has exfoliated and cracked at this point, as shown in Fig. 6(a), and the film rupture potential is the corresponding potential. The exfoliated passive film has a yellow-green tint due to the addition of various corrosion products. In addition, the large-area exfoliated passive film was crushed after the experiment. As shown in Fig. 6(b), after removing the corrosion products, some black debris is deposited on the bottom of the container of the experimental device.

3.2. AE signal analysis

The AE signal is also being captured simultaneously (Smanio et al., 2011). High potential causes the specimen surface to quickly oxidize into film, shatter, and begin the pitting stage. The variations in impact rate and signal amplitude distribution tracked by an AE acquisition system every 100 s are shown in Fig. 7 and Fig. 8.

Three controlled experiments were established and their hits were comparable in this study, as shown in Fig. 7. As illustrated in Fig. 8, the pitting corrosion process can be loosely split into three stages based on the activity of the AE signal. Among them, 0 to 800 s is the activation response and passive film rupture stage, and during the 0 to 600 s activation reaction stage, the specimen dissolves and oxidizes into a film in a highly potential acidic corrosive solution. The conflict between metal dissolution and oxidation film formation is evident throughout the passivation film formation process due to the high activation reaction occurring at this time. As a result, the experiment's signal activity is substantially higher in the early stages than it is in the later stages, and the signal is constant during this time. The created passive film partially exfoliates under high potential and ruptures quickly at the 400 to 800 s passivation film's rupture stage, causing an abrupt rise in hits. Cl^- has not demonstrated obvious advantages in competition with oxygen during the 500 to 2300 s corrosion pit propagation stage after passive film rupture, the pitting reaction is slow, the pit is in the propagation phase, and signal activity is reduced. In the following pitting reaction stage, Cl^- adsorption has obvious advantages, the pitting reaction is intense, and signal activity is increased. The frequency of hits occasionally spikes during the pitting reaction stage, and assumed that when the corrosion product accumulates to a particular amount, a specific behavior causes it to produce a lot of signals.

Fig. 7 and Fig. 8 can be well-corresponded. The breaking of the passive film and substantial activation reaction occurs between 0 s and 500 s. The AE signal has a high amplitude, typically between 45 dB and 55 dB. The corrosion pit propagation stage lasts for 500 to 1700 s, and the AE signal's amplitude is less than 45 dB. The pitting reaction stage starts after the 1700 s, indicating that the amplitude of the signal created by pitting corrosion is typically higher than that generated by uniform corrosion because the amplitude range of the AE signal is rich at this time and a large number of high amplitude signals above 55 dB occur.

Five fundamental AE signal characteristics, amplitude, count, duration time, rising time, and absolute energy, are retrieved based on fundamental signal processing. Then, using mathematical

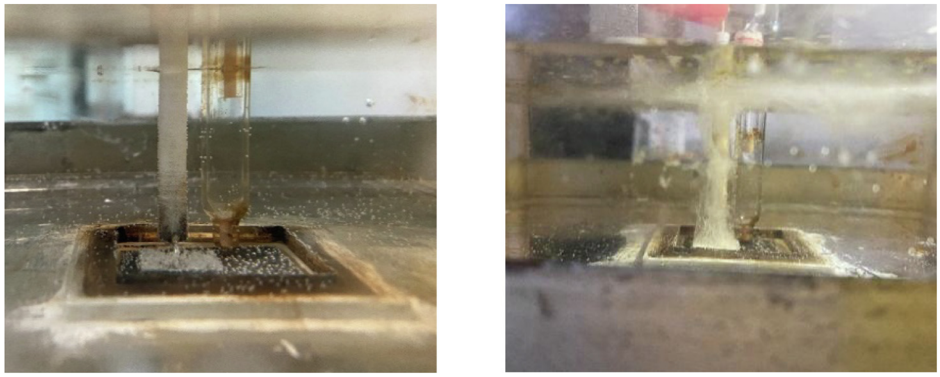

(a) a small number of bubbles	(b) a large number of bubbles

Fig. 5. Bubble generation during potentiodynamic polarization of X90 steel.

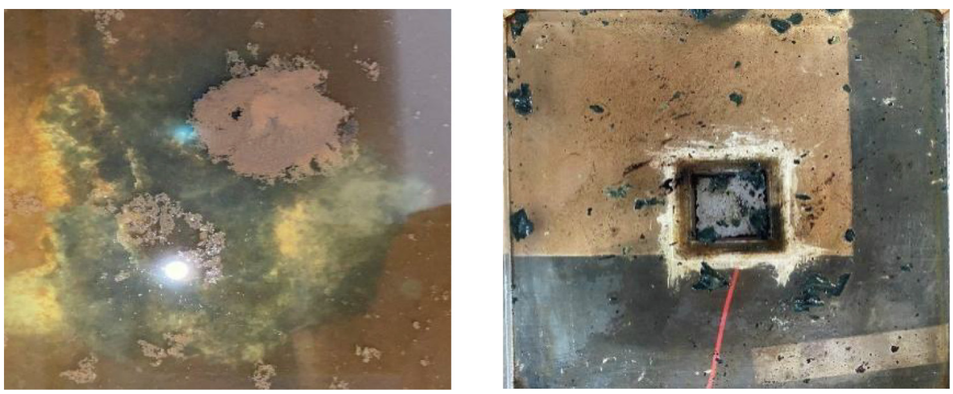

(a) passive film exfoliation in the experiment	(b) passive film rupture after the experiment

Fig. 6. Exfoliation and rupture of the passive film.

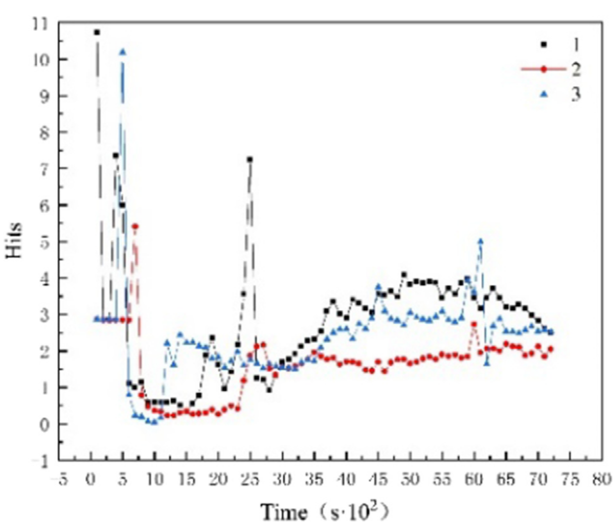

Fig. 7. Average AE hits rate.

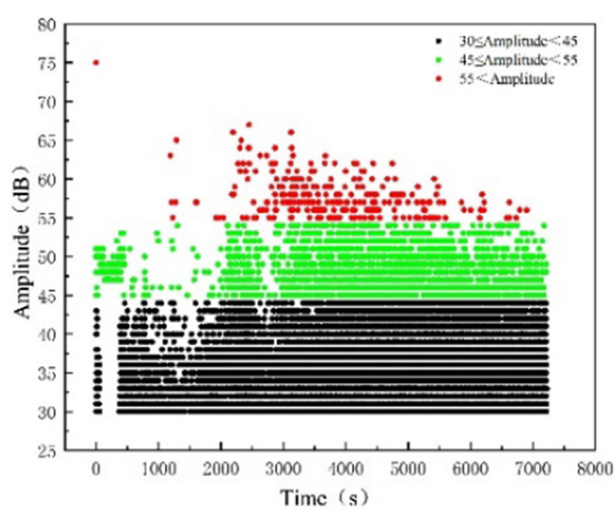

Fig. 8. Hits vs. time distribution of pitting signal per 100 s.

methods, the underlying structure of the signal data is explored and classified. The similarity dimension reduction approach is suggested and the Pearson formula is used to reject the overly high similarity between variables to prevent the issue of "dimension disaster" in the computation of multidimensional parameters (Bellman, 1966; Li et al., 2022; Barile et al., 2022).

$$K = \frac{\sum_{i=1}^{m}\left(X_i - \bar{X}\right)\left(Y_i - \bar{Y}\right)}{\sqrt{\sum_{i=1}^{m}\left(X_i - \bar{X}\right)^2}\sqrt{\sum_{i=1}^{m}\left(Y_i - \bar{Y}\right)^2}} \quad (1)$$

where $\bar{X}$, $\bar{Y}$ are the average value of a variable.

The acquired five characteristic parameters of pitting AE signal are taken into Formula (1) to perform Pearson correlation analysis. The calculated results are shown in Table 2:

The correlation coefficients between count, duration, and absolute energy are all more than 0.9, as can be seen in Table 2. The quantity of model calculation will exponentially rise if the coefficients are included, which is bad for the precision of the clustering results. From the AE parameter, it is clear that the differences in absolute energy between stages are more pronounced than those in count and duration time. As a result, the absolute energy, amplitude, and retention rising time are clustering variables. The magnitudes of the three sets of data are very varied, hence the results of the clustering are likely to be very different from the actual circumstance. To ensure that the sample data are on the same scale, the data samples require Z-score normalization. The following is the Z-score algorithm:

$$Z = \frac{x - \mu}{s} \quad (2)$$

where x is each eigenvalue of the data to be processed;μ is the Arithmetic average value of feature parameters to be processed; s is the Standard deviation of characteristic parameters to be processed.

Due to a large number of signal data and the difference in AE sources in each stage, the signals in different stages are clustered separately (Ramasso et al., 2022; Pei et al., 2021; Saha and Vidya, 2021). Through the K-means clustering algorithm by using SPSS software. The clustering method is based on the clustering algorithm of sample set division, and the iterative method is adopted to obtain the local optimal solution. The pre-processed characteristic parameter data are imported into SPSS software and the results are shown in Fig. 9, Fig. 10, and Fig. 11.

As can be seen from Fig. 9, signals in the activation reaction and film rupture stage are divided into 2 classes. In class 1, signals are mainly generated by metal activation reaction and film generation, and most of the characteristic parameter values are relatively low, with the amplitude below 50 dB, while a few of the characteristic parameter values are relatively high during passivation film generation. The proportion of class 2 signal is higher, and its AE source is mainly passivated film rupture, and its amplitude is mainly concentrated at about 50 dB, and its rise time range is wide, and its distribution is 0 to 80000 μs, and its absolute energy is concentrated between 250,000 aJ and 550,000 aJ.

As shown in Fig. 10, and found that the corrosion pit propagation stage is well divided into 3 types of signals, of which the number of class 1 signals is relatively small, but their amplitude and absolute energy are relatively high. Most of them are within 500 aJ and a few can be up to about 3000 aJ. It is considered that some corrosion pits have occurred violent pitting reactions. The amplitude of the class 2 signal is mostly less than 40 dB, and the absolute energy is less than 90 aJ, but its rising time range is wide. It is considered that this kind of signal is generated by corrosion pit propagation. Class 3 signals are mainly concentrated in the vicinity of 30 dB and 40 to 45 dB, and their absolute energy is higher than that of class 2 signals, up to about 300aJ, but class3 rising time is

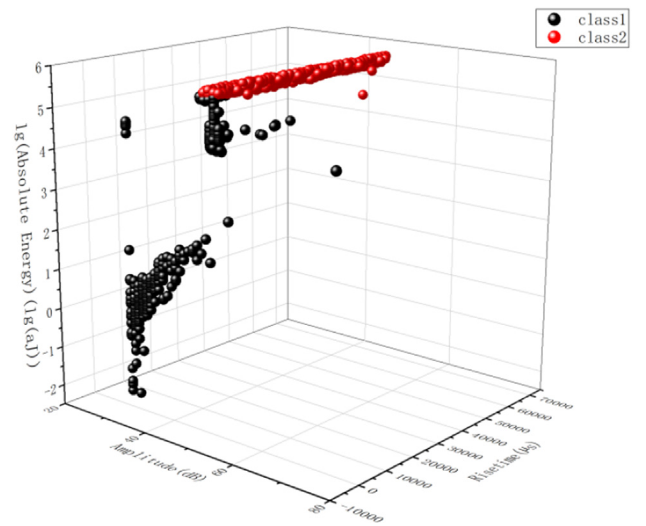

Fig. 9. Three-dimensional graph of absolute energy-amplitude-rise time in activation reaction and film rupture stage.

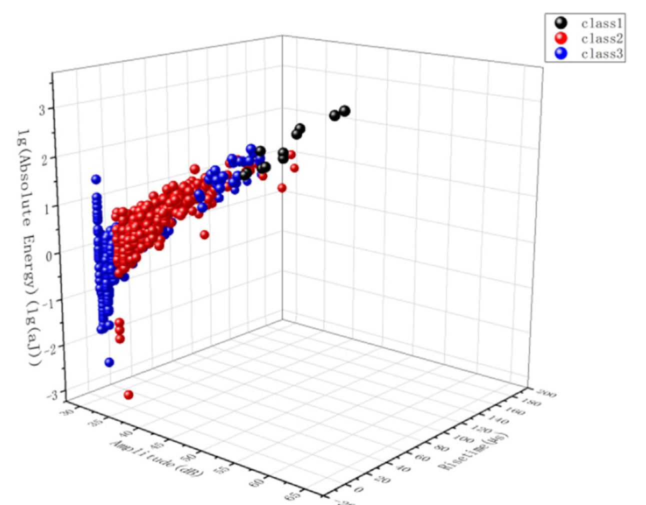

Fig. 10. Three-dimensional graph of absolute energy-amplitude-rise time during the corrosion pit propagation stage.

Table 2
Correlation coefficient of pitting signal characteristic parameters.

	Rise time	Count	Duration time	Amplitude	Absolute energy
Rise time	1	0.766	0.829	0.241	0.812
Count	0.766	1	0.959	0.448	0.961
Duration time	0.829	0.959	1	0.346	0.986
Amplitude	0.241	0.448	0.346	1	0.361
Absolute energy	0.812	0.961	0.986	0.361	1

shorter. It is considered that the signals are mainly generated by the activities of corrosion products.

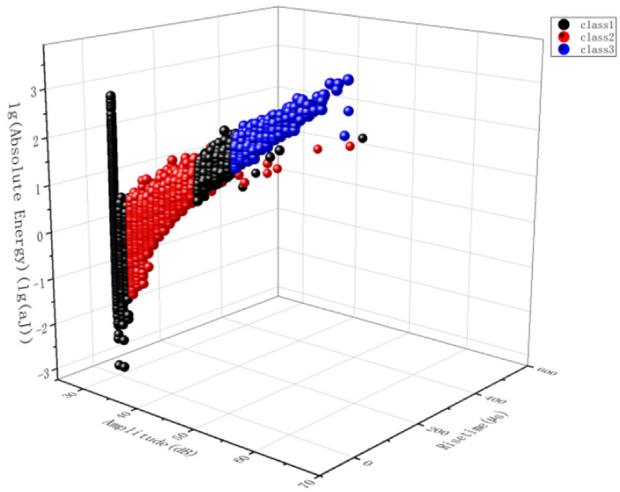

Fig. 11. Three-dimensional graph of absolute energy-amplitude-rise time in pitting reaction stage.

Similar to the classification used in the stage of corrosion pit propagation, the signal in the pitting reaction stage is classified. It is classified into three groups and the source of AE is the same, as shown in Fig. 11. As can be observed, there are more signals in the category of high absolute energy signals, and some of these signals have absolute energies as high as 6000 aJ. This is due to the pitting reaction being more extreme. Because more corrosion products are created by violent corrosion reactions and because the exfoliation and friction activities are more intense, the absolute energy of the signal produced by the corrosion product activity is also higher than that of the previous stage.

3.3. AE signal time–frequency analysis

Fig. 12, Fig. 13, and Fig. 14 are typical signals in different stages, which can reflect the corrosion characteristics of this stage. In the stage of activation reaction and film rupture, the two signal waveforms shown in Fig. 12 are dominant, and the proportion of signals as shown in Fig. 12(a) is larger. The main source of AE is the passivation film rupture, which is characterized by an upward trend in the waveform, high amplitude, and long duration (Zhang and Li, 2020; Wu et al., 2021). In the frequency domain, the frequency range is mainly concentrated in 50 to 200 kHz with high amplitude. The peak frequency is about 5.2 × 10^{-3} V and the peak fre-

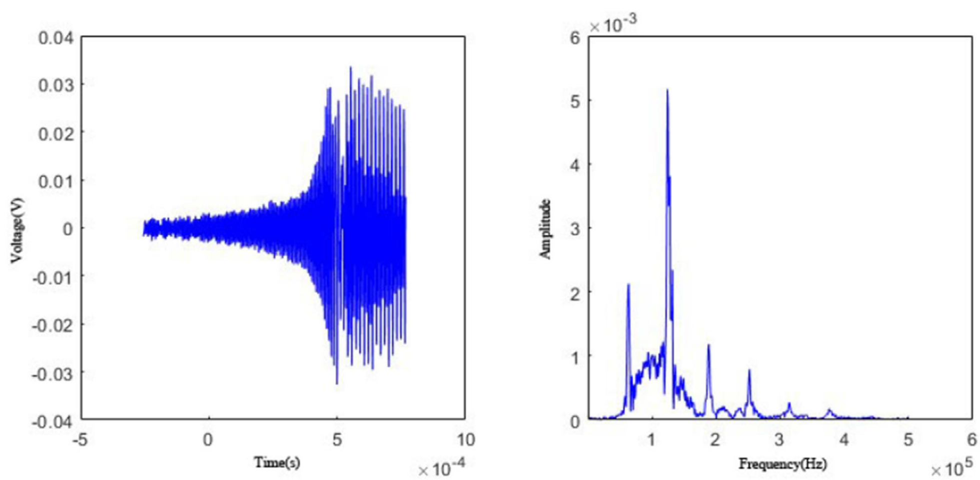

(a) Signal waveform 1

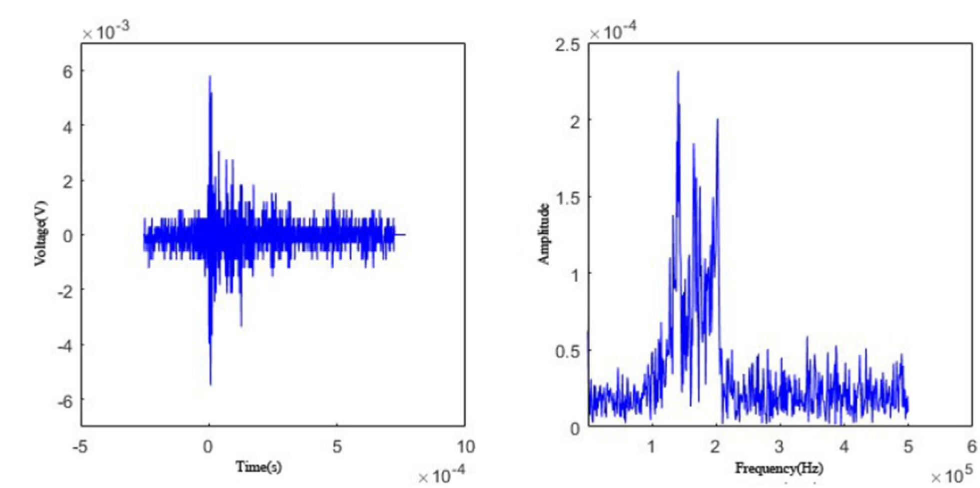

(b) Signal waveform 2

Fig. 12. Waveform characteristics of the activation reaction and film rupture stage.

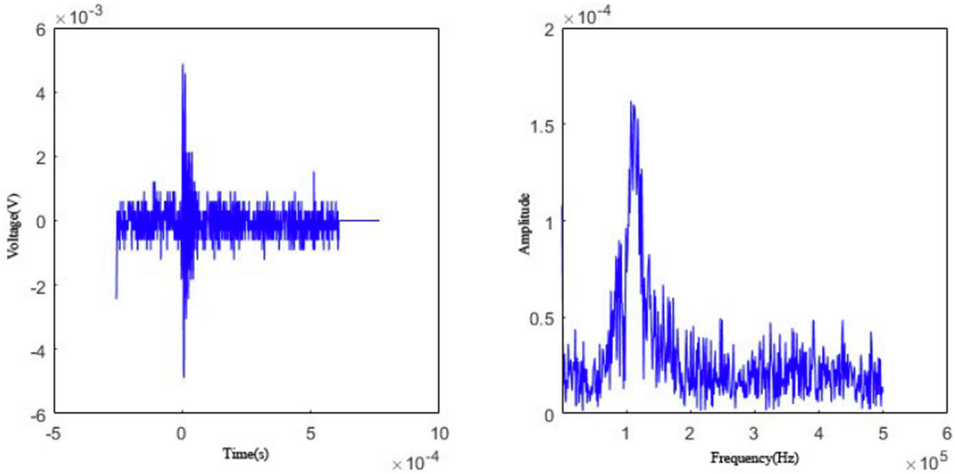

(a) Signal waveform 1

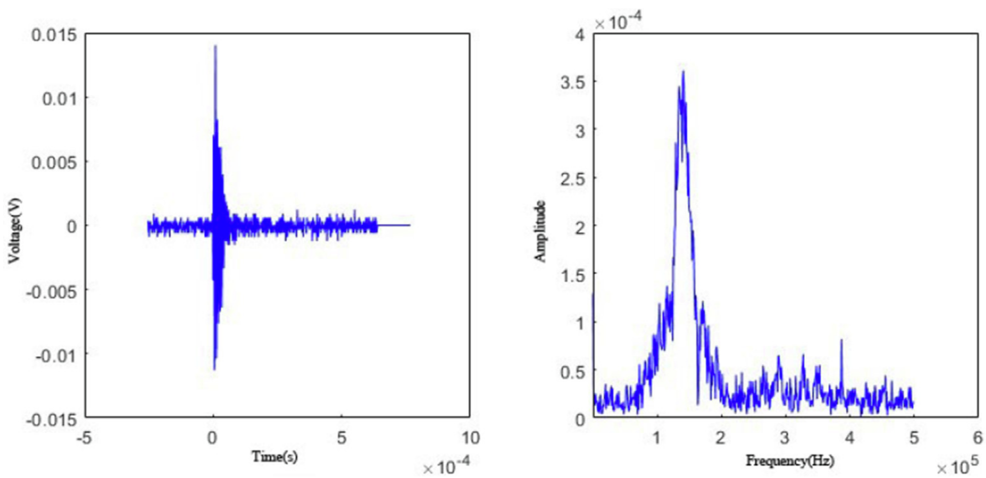

(b) Signal waveform 2

Fig. 13. Waveform characteristics of the corrosion pit propagation stage.

quency is about 175 kHz. The signal shown in Fig. 12(b) is mainly generated by the oxidation reaction of metal and is characterized by low amplitude and short duration in the time domain. Compared with the signal shown in Fig. 12(a), the frequency range is narrower and the amplitude is lower, with a peak value of about 2.3×10^{-4} V and a peak frequency of about 175 kHz. In the corrosion pit propagation stage, the two signals shown in Fig. 13 are mainly used. The two signals show similar characteristics to the signals as shown in Fig. 12(b) in the frequency domain, but shorter in the time domain than the signals as shown in Fig. 12(b). The main difference between the two signals is the difference in amplitude. The signal amplitude as shown in Fig. 13(a) is of the same order of magnitude as that shown in Fig. 13(b), which is about 5×10^{-3} V. The signal amplitude as shown in Fig. 13(b) is higher, which is about 1.5×10^{-2} V. In the pitting reaction stage, three signals are dominant, as shown in Fig. 12. The signals as shown in Fig. 14(a) and Fig. 14 (b) are the same as those in the corrosion pit propagation stage. These signals are mainly generated by corrosion pit propagation and corrosion product activity, while the signals as shown in Fig. 14(c) are special, mainly by strong pitting reactions, with the smallest proportion among them. Its signal waveform parameters are close to the signal as shown in Fig. 12 (a), with an amplitude of about 5×10^{-2} V. In the frequency domain, the frequency range is concentrated in 50 to 200 kHz, and the peak frequency is around 100 kHz. Compared with the signal as shown in Fig. 12(a), it has a shorter duration and simpler frequency composition.

3.4. AE signal wavelet analysis

3.4.1. Wavelet de-noising

The signals from several AE sources were de-noised using the db4 wavelet, which was chosen using the programming software MATLAB (Zitto et al., 2015; Zhang et al., 2021; Barile et al., 2019; Sheikh et al., 2021; Lin et al., 2023). Fig. 15 compares the pitting reaction signal de-noising and corrosion pit propagation of X90 steel. As can be observed, the pitting signal's amplitude characteristic weakens after de-noising, the signal becomes smoother, and the faint second peak feature manifests itself in the frequency domain.

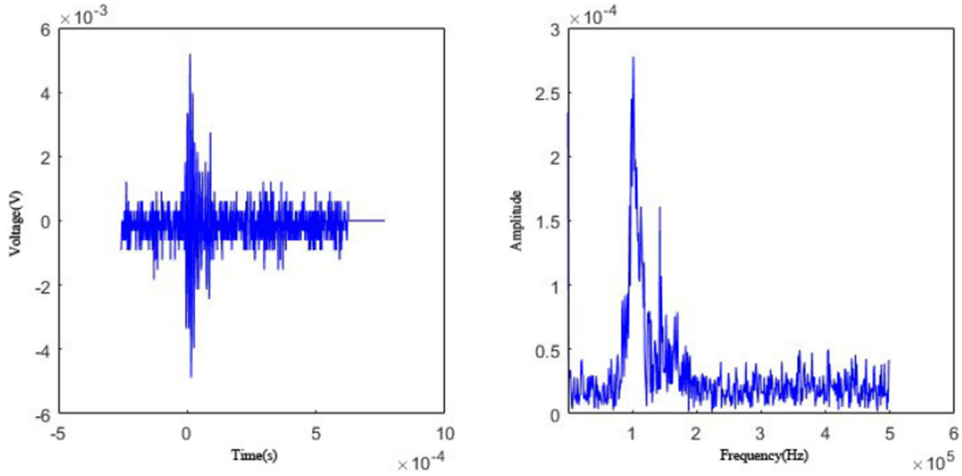

(a) Signal waveform 1

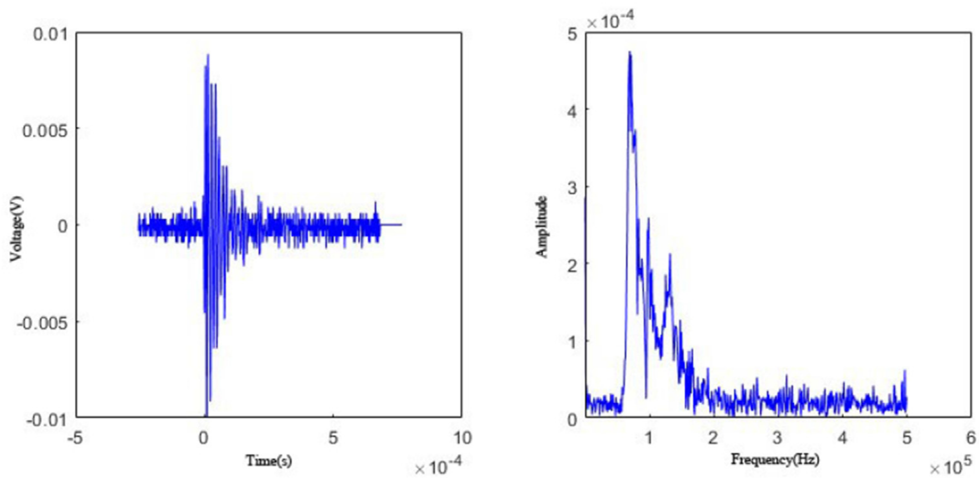

(b) Signal waveform 2

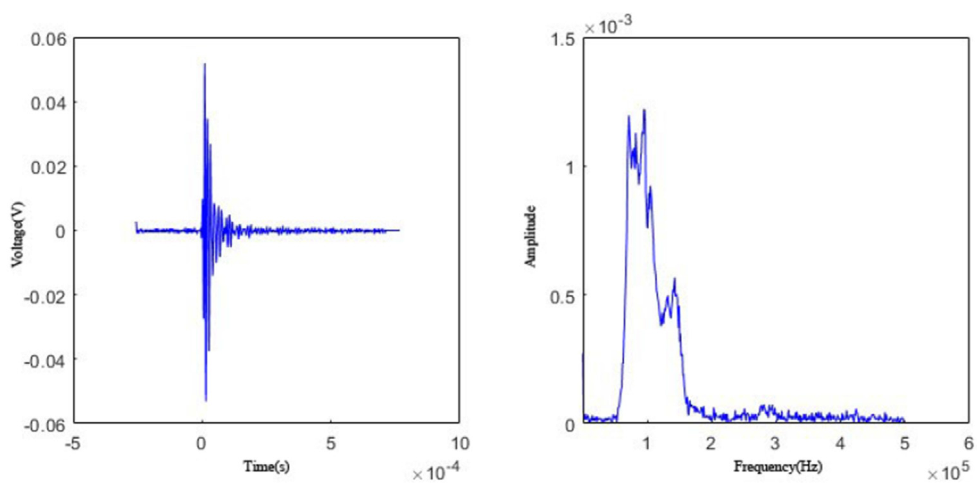

(c) Signal waveform 3

Fig. 14. Waveform characteristics of the pitting reaction stage.

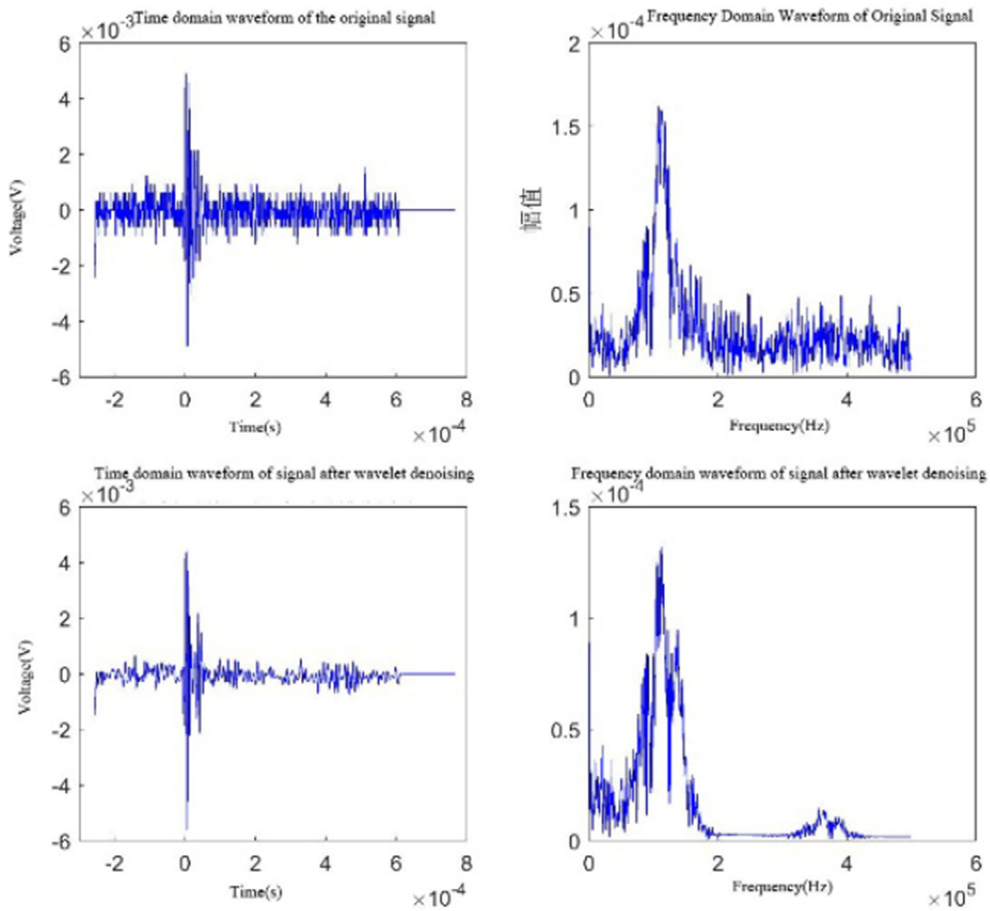

Fig. 15. Comparison of corrosion pit propagation and pitting reaction signal de-noising of X90 steel before and after.

3.4.2. Wavelet decomposition and reconstruction

The signal can be decomposed into sub-signals of each frequency band through wavelet decomposition, and signal reconstruction and feature extraction can be effectively carried out. The wavelet reconstruction is the inverse process of the wavelet decomposition, i.e. the sub-signals processed after decomposition are restored to facilitate the subsequent signal analysis. The denoising signal is decomposed in five stages by programming with MATLAB software, as shown in Fig. 16. It can be found from the figure that the cd3 component coefficient of the pit propagation and pitting reaction signal is consistent with the reconstructed component characteristic. The single-branch reconstruction of the signal is shown in Fig. 17. Compared with the original signal, the reconstructed signal has a great difference in the time domain, and in the frequency domain, the small amplitude noise signal is eliminated, making the research signal pure.

3.5. Electrochemical impedance spectroscopy analysis

The EIS (electrochemical impedance spectroscopy) of X90 steel at different periods is shown in Fig. 18. It can be seen from the diagram that the impedance spectra of the pitting experiments show a single capacitive reactance arc feature (Fu et al., 2021; Pejcic and De Marco, 2006). The order of capacitive reactance arc radius is 0 s > 2000 s > 7200 s > 500 s with time. The radius of the capacitive reactance arc is negatively correlated with the corrosion rate; and the radius of the capacitive reactance arc is greatest at 0 s. At this point, the potential has not been introduced into the experimental device system and the corrosion rate is very small. After potentiostatic polarization, the specimen enters the stage of activation reaction and film rupture, and dissolves rapidly, and increases the corrosion rate. This stage is the largest corrosion rate in the entire pitting corrosion experiment. Therefore, the radius of the capacitive reactance is the smallest. After the passivation film rupture, the corrosion of the specimen enters the corrosion pit propagation stage. At this time, there is less Cl^- adsorbed on the specimen and the corrosion is slow. Therefore, the radius of the capacitive reactance becomes larger. After the 2000 s, the specimen enters the active period of pitting reaction, and the corrosion rate increases, and the radius of the capacitive reactance decreases.

3.6. Morphological characteristics of the pitting process in X90 steel

The specimen was examined under a microscope at 450 times magnification after a minor rust removal treatment of the surface, and Fig. 19 depicts the pitting morphology. The surface of the specimen clearly displayed the “large cathode-small anode” phenomenon after the pitting experiment. Based on the figure, it appears that the pits are shallow but are developing in a downward trend. According to statistics, the average diameter of the pits is between 22.2 and 33.3 μm.

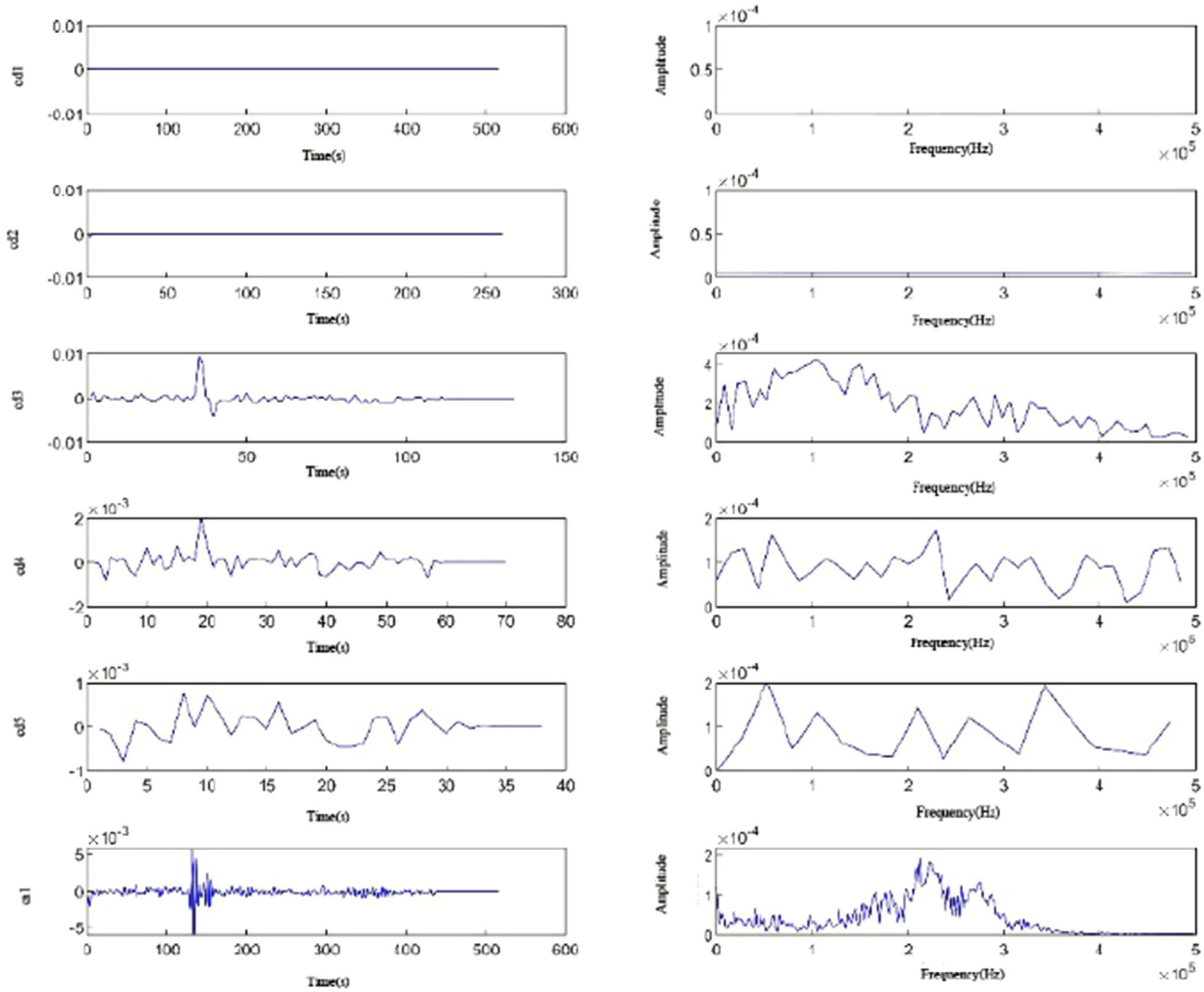

Fig. 16. Signal components and spectra of corrosion pit propagation and pitting reaction of X90 steel.

4. Conclusions

Test equipment for AE electrochemistry was built. The properties of the AE signal and changes in electrochemical parameters were measured by using a potential voltage of 1.3 V for two hours. These are the conclusions:

(1) Three steps can be identified in the pitting of X90 steel: activation response and passive film rupture, corrosion pit propagation, and pitting reaction.
(2) The signal produced by the rupture of the passive film exhibits distinct properties in the time–frequency analysis of the AE signal. It is a continuous signal that is both more powerful and lasts longer than the signal produced by an oxidation reaction. The frequency band primarily focuses on the range of 50 to 200 kHz, with 175 kHz as its peak frequency. The oxidation reaction's signals, which differ primarily in amplitude and length, are identical to those of the pit propagation stage and the pitting reaction stage in the spectrum. The powerful reaction during the pitting stage also results in a few unique indications. The waveform and spectrum properties of the powerful pitting stage reaction closely resemble those of the film rupture signal.
(3) After the signal is decomposed and reconstructed in 5 stages, the small signal outside the signal frequency band disappears, which makes the characteristics of corrosion signal attenuation more outstanding.

Declaration of Competing Interest

The authors declare that they have no known competing financial interests or personal relationships that could have appeared to influence the work reported in this paper.

Acknowledgments

This research was supported by the Natural Science Foundation of Shandong Province, China (Grant No. ZR2017BEE068), the Opening fund of Shandong Key Laboratory of Oil & Gas Storage and Transportation Safety, and the Fundamental Research Funds for Central Universities (19CX05007A).

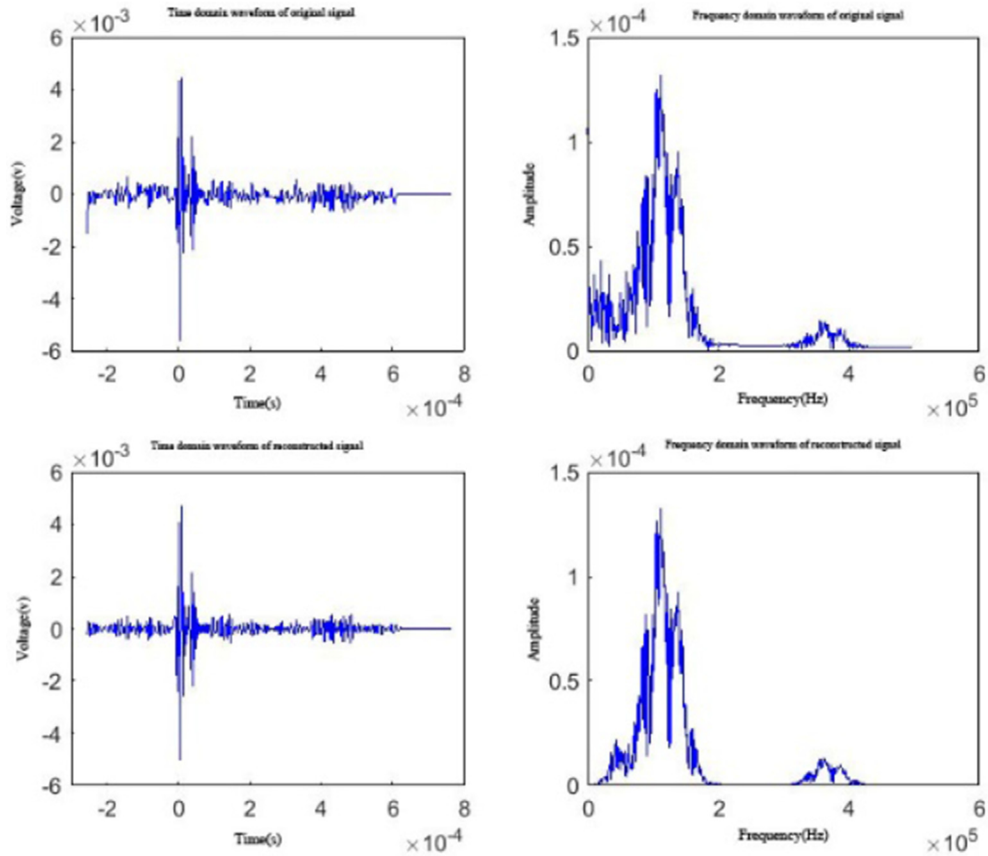

Fig. 17. Comparison of corrosion pit propagation and pitting reaction signal reconstruction of X90 steel.

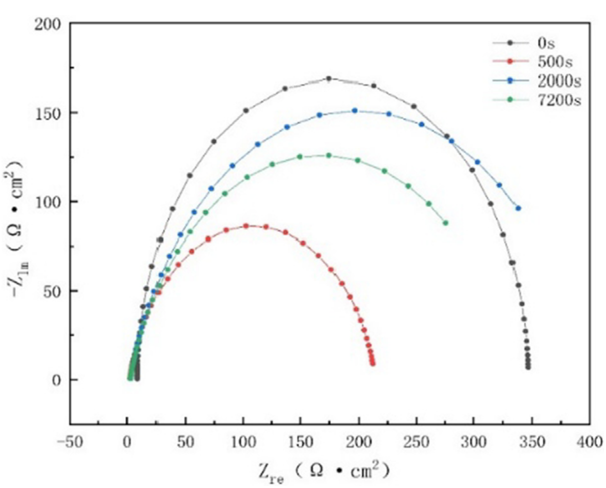

Fig. 18. EIS of X90 steel pitting test in different periods.

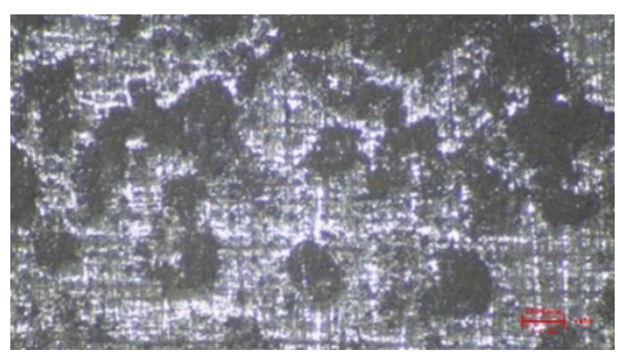

Fig. 19. Microscopic pitting morphology of X90 steel.

References

Barile, C., Casavola, C., Pappalettera, G., Vimalathithan, P.K., 2019. Experimental wavelet analysis of acoustic emission signal propagation in CFRP. Eng. Fract. Mech. 210, 400–407.

Barile, C., Casavola, C., Pappalettera, G., Paramsamy, K.V., 2022. Laplacian score and K-means data clustering for damage characterization of adhesively bonded CFRP composites by means of acoustic emission technique. Appl. Acoust. 185, 108425.

Bellman, R., 1966. Dynamic programming and the quadratic form of Selberg. J. Math. Anal. Appl. 15, 30–32.

Bhardwaj, U., Teixeira, A.P., Guedes, S.C., 2021. Burst strength assessment of X100 to X120 ultra-high strength corroded pipes. Ocean Eng. 241, 110004.

Bi H, Li H, Yun Z, Zhao S, Zhang X, Chou P, et al. An on-line acoustic emission - electrochemical joint experimental device for stress corrosion of tank floor.

Chen, M., Li, N., Mu, H., 2021. Assessment of a low-carbon natural gas storage network using the FLP model: a case study within China-Russia natural gas pipeline East Line's coverage. J. Nat. Gas Sci. Eng. 96, 104246.

Dai, M., Liu, J., Huang, F., Zhang, Y., Cheng, Y.F., 2018. Effect of cathodic protection potential fluctuations on pitting corrosion of X100 pipeline steel in acidic soil environment. Corros. Sci. 143, 428–437.

Eliyan, F.F., Mohammadi, F., Alfantazi, A., 2012. An electrochemical investigation on the effect of the chloride content on CO_2 corrosion of API-X100 steel. Corros. Sci. 64, 37–43.

Feng, L., Huang, D., Chen, X., Shi, H., Wang, S., 2021. Residual ultimate strength investigation of offshore pipeline with pitting corrosion. Appl. Ocean Res. 117, 102869.

Feng, Y., Ji, L., Chen, H., Jiang, J., Wang, X., Ren, Y., et al., 2021. Research progress and prospect of key technologies for high-strain line pipe steel and pipes. Nat. Gas Ind. B 8, 146–153.

Fregonese, M., Idrissi, H., Mazille, H., Renaud, L., Cetre, Y., 2001. Initiation and propagation steps in pitting corrosion of austenitic stainless steels: monitoring by acoustic emission. Corros. Sci. 43, 627–641.
Fu, J.-d., Wan, S., Yang, Y., Su, Q., Han, W.-w., Zhu, Y.-b., 2021. Accelerated corrosion behavior of weathering steel Q345qDNH for bridge in industrial atmosphere. Constr. Build. Mater. 306, 124864.
Ju, H., Liu, S., Zhang, W., Yang, Y., Duan, J., 2021. Investigation of pitting corrosion and hydrogen evolution of aluminum and AA2024 alloy by simultaneous electrochemical measurements and imaging. Electrochem. Commun. 132, 107135.
Li, L., Chen, X., Song, C., 2022. A robust clustering method with noise identification based on directed K-nearest neighbor graph. Neurocomputing 508, 19–35.
Li, J., Lin, B., Zheng, H., Wang, Y., Zhang, H., Zhang, Y., Nie, Z., Tang, J., 2023. Study on pitting corrosion behavior and semi in-situ pitting corrosion growth model of 304 L SS with elastic stress in NaCl corrosion environment. Corros. Sci. 211, 110862.
Lin, J., Zhou, W., Cui, X.Z., Hong, H.P., 2023. Application of wavelet transforms to the simulation of corrosion fields on buried pipelines. Comput. Struct. 276, 106957.
Luguang, L., 2022. Development of natural gas industry in China: Review and prospect. Nat. Gas Ind. B 9, 187–196.
Luo, J., Zhang, L., Li, L., Yang, F., Ma, W., Wang, K., et al., 2016. Electrochemical corrosion behaviors of the X90 linepipe steel in NS4 solution. Nat. Gas Ind. B 3, 346–351.
Luo, J., Luo, S., Li, L., Zhang, L., Wu, G., Zhu, L., 2019. Stress corrosion cracking behavior of X90 pipeline steel and its weld joint at different applied potentials in near-neutral solutions. Nat. Gas Ind. B 6, 138–144.
Pei, N., Zhou, S., Xu, C., Shang, J., Wu, Q., 2021. Cluster analysis of acoustic emission signals for tensile damage characterization of quasi-static indented carbon/glass fiber-reinforced hybrid laminate composites. Compos. A Appl. Sci. Manuf. 150, 106597.
Pejcic, B., De Marco, R., 2006. Impedance spectroscopy: Over 35 years of electrochemical sensor optimization. Electrochim. Acta 51, 6217–6229.
Ramasso, E., Denœux, T., Chevallier, G., 2022. Clustering acoustic emission data streams with sequentially appearing clusters using mixture models. Mech. Syst. Sig. Process. 181, 109504.
Saha, I., Vidya, S.R., 2021. Classification of the acoustic emissions generated during the tensile fracture process in steel fibre reinforced concrete using a waveform-based clustering method. Constr. Build. Mater. 294, 123541.
Seghier, E.A.B.M., Keshtegar, B., Tee, K.F., Zayed, T., Abbassi, R., Trung, N.T., 2020. Prediction of maximum pitting corrosion depth in oil and gas pipelines. Eng. Fail. Anal. 112, 104505.
Sheikh, M.F., Kamal, K., Rafique, F., Sabir, S., Zaheer, H., Khan, K., 2021. Corrosion detection and severity level prediction using acoustic emission and machine learning based approach. Ain Shams Eng. J. 12, 3891–3903.
Smanio, V., Fregonese, M., Kittel, J., Cassagne, T., Ropital, F., Normand, B., 2011. Contribution of acoustic emission to the understanding of sulfide stress cracking of low alloy steels. Corros. Sci. 53, 3942–3949.
Tan, Z., Yang, L., Zhang, D., Wang, Z., Cheng, F., Zhang, M., et al., 2020. Development mechanism of internal local corrosion of X80 pipeline steel. J. Mater. Sci. Technol. 49, 186–201.
Wang, G., Cheng, Q., Zhao, W., Liao, Q., Zhang, H., 2022. Review on the transport capacity management of oil and gas pipeline network: Challenges and opportunities of future pipeline transport. Energ. Strat. Rev. 43, 100933.
Wang, Z., Kong, Y., Li, W., 2022. Review on the development of China's natural gas industry in the background of "carbon neutrality". Nat. Gas Ind. B 9, 132–140.
Wu, K., Kim, J.-Y., 2021. Acoustic emission monitoring during open-morphological pitting corrosion of 304 stainless steel passivated in dilute nitric acid. Corros. Sci. 180, 109224.
Wu, Y., Nong, J., Yuan, S., Guo, Q., Xu, J., 2021. Acoustic emission behaviour during the evolution of a single pit on stainless steels. Corros. Sci. 183, 109308.
Xu, J., Wu, X., Han, E.-H., 2011. Acoustic emission during pitting corrosion of 304 stainless steel. Corros. Sci. 53, 1537–1546.
Zhang, X., Li, B., 2020. Damage characteristics and assessment of corroded RC beam-column joint under cyclic loading based on acoustic emission monitoring. Eng. Struct. 205, 110090.
Zhang, Y., Shi, J., Zheng, J., 2021. A method of fracture toughness JIC measurement based on digital image correlation and acoustic emission technique. Mater. Des. 197, 109258.
Zhang, Z., Zhao, Z., Bai, P., Li, X., Liu, B., Tan, J., et al., 2021. In-situ monitoring of pitting corrosion of AZ31 magnesium alloy by combining electrochemical noise and acoustic emission techniques. J. Alloy. Compd. 878, 160334.
Zitto, M.E., Piotrkowski, R., Gallego, A., Sagasta, F., Benavent-Climent, A., 2015. Damage assessed by wavelet scale bands and b-value in dynamical tests of a reinforced concrete slab monitored with acoustic emission. Mech. Syst. Sig. Process. 60–61, 75–89.